Journal of Loss Prevention in the Process Industries 84 (2023) 105135

Contents lists available at ScienceDirect

Journal of Loss Prevention in the Process Industries

journal homepage: www.elsevier.com/locate/jlp

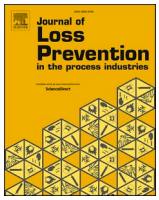

Modelling breakdown of industrial thermal insulation during fire exposure

Amalie Gunnarshaug [a,b,*], Torgrim Log [c,d], Maria-Monika Metallinou [c], Trygve Skjold [b]

[a] Q Rådgivning AS, Øvregata 126, 5527, Haugesund, Norway
[b] Department of Physics and Technology, University of Bergen, 5020, Bergen, Norway
[c] Fire Disasters Research Group, Department of Safety, Chemistry and Biomedical Laboratory Sciences, Western Norway University of Applied Sciences, 5528, Haugesund, Norway
[d] Gassco Inc., Bygnesvegen 75, 4250, Kopervik, Norway

ARTICLE INFO

Keywords:
Thermal insulation
Fire exposure
Thermal conductivity
Heat transfer
Elevated temperatures
Numerical model

ABSTRACT

The aging of many of the installations in the oil and gas industry may increase the likelihood of loss of containment of flammable substances, which could lead to major accidents. Flame temperatures in a typical hydrocarbon fire may reach 1100–1200 °C, which are associated with heat flux levels between 250 and 350 kW/m^2. To limit or delay the escalation of an initial fire, passive fire protection (PFP) can be an effective barrier. Additionally, both equipment and piping may require thermal insulation for heat or cold conservation. Previous studies have investigated whether thermal insulation alone may protect the equipment for a required time period, e.g., until adequate depressurization is achieved. The present study entails the development of a numerical model for predicting the heat transport through a multi-layer wall of a distillation column exposed to fire. The outer surface is covered by stainless-steel weather protective cladding, followed by PFP, thermal insulation, and finally an inner column of carbon steel of variable thicknesses. The model for the breakdown of thermal insulation is based on observed dimensional changes and independent measurements of the thermal conductivity of the insulation after heat treatment. The calculated temperature profiles of thermally insulated carbon steel during fire exposure are compared to fire test results for carbon steel with thicknesses of 16, 12, 6 and 3 mm. The model's predictions agree reasonably well with the experiments. The degradation of the thermal insulation at temperatures above 1100 °C limits its applicability as fire protection, especially for low carbon-steel thickness. However, the model predicts that adding a 10-mm layer of more heat-resistant insulation (PFP) inside the fire-exposed cladding may considerably extend the time to breakdown of the thermal insulation.

1. Introduction

The oil and gas industry involves equipment containing flammable gases and liquids; loss of containment and subsequent ignition represent a significant hazard. Two severe fires have occurred in this industry in Norway in recent years, i.e., the fire at the Hammerfest LNG (Liquified Natural Gas) plant on September 28, 2020 (Bakka et al., 2021; Hallan et al., 2021; Log and Gunnarshaug, 2022) and the fire at the Tjeldbergodden methanol plant on 2nd December 2020 (Handal et al., 2021; Landro et al., 2021). Containment of the inventory of equipment and piping is important, to avoid a potential incident or escalation of an incident (Equinor, 2020). The use of passive fire protection (PFP) can prevent, or significantly delay, rupture of equipment exposed to fire loads. In addition, thermal insulation is often required to maintain a certain operating temperature (Bahadori, 2014; Scandpower, 2004; Standard Norway, 2018). Thus, a process equipment configuration, e.g., a distillation column, will typically consist of stainless-steel weather protective cladding, PFP, thermal insulation and a carbon-steel process equipment body.

The aging facilities in the oil and gas industry are subject to regular inspections. These have revealed severe corrosion attacks, especially in situations where the thermal insulation is in direct contact with the carbon-steel surface (API, 2014).

To avoid direct contact between the metal surface and the thermal insulation, and thereby prevent corrosion, current insulation methods apply spacers, typically made from polytetrafluoroethylene (PTFE), and a perforated metal plate, to create an airgap of typically 25 mm between the metal surface and the thermal insulation. A representative

* Corresponding author. Q Rådgivning AS, Øvregata 126, 5527, Haugesund, Norway.
E-mail addresses: amg@qrad.no (A. Gunnarshaug), tlog@gassco.no, torgrim.log@hvl.no (T. Log), monika.metallinou@hvl.no (M.-M. Metallinou), Trygve.Skjold@uib.no (T. Skjold).

https://doi.org/10.1016/j.jlp.2023.105135
Received 28 April 2023; Received in revised form 16 June 2023; Accepted 9 July 2023
Available online 12 July 2023

distillation column is illustrated in Fig. 1. The layer of thermal insulation is typically 50 mm thick, followed by a 50-mm layer of PFP. An outer layer of 0.7-mm-thick stainless-steel cladding provides weather protection.

The introduction of the 25-mm airgap, with unaltered thicknesses of insulation, increases the outer diameter of the equipment by 50 mm. In a densely packed process plant, there may not be room for this. Use of excessive fire protection should be avoided and only be provided where strictly necessary (Choi and Beyeon, 2021).

Previously published small-scale testing of a mock-up of a distillation column wall has shown that 50 mm of thermal insulation alone can provide sufficient fire protection for a 16-mm carbon-steel wall (Bjørge et al., 2017, 2018). The small-scale test setup and the thermal insulation after a test are shown in Fig. 2. When exposed to high temperatures (1200 °C+), the insulation is sintered and partly melted, resulting in cracks. The thermal insulation after muffle furnace tests, where 50-mm cubes (a-d) and a 75-mm cube (e) have been heated to temperatures between 700 °C and 1200 °C, is shown in Fig. 3 (Bjørge et al., 2018; Gunnarshaug et al., 2020, 2021). The remains of the thermal insulation had a stone-like texture.

Previous studies have revealed an exothermic peak at about 800–900 °C in muffle oven heating tests and TGA (Thermal gravimetric analysis)/DSC (Differential Scanning Calorimetry) measurements (Bjørge et al., 2018; Gunnarshaug et al., 2020). Such a peak has also been observed for similar materials (Olsen et al., 2013; Ozawa, 1971; Shao et al., 2004; Sjöström and Jansson, 2012). It is important to account for the potential contribution of this peak to the temperature development in the total system during fire exposure. Lai et al. (2020) and Shao et al. (2004) investigated the crystallization kinetics of similar ceramics and found activation energies in the range of 225–300 kJ/mol depending on the composition of the material.

Fire testing can be expensive and time-consuming, and a numerical model that can reliably predict the temperature development can be a valuable tool for evaluating whether thermal insulation alone provides sufficient protection. It could also allow the combined performance of thermal insulation and PFP to be evaluated. Thus, the aim of the present study was to develop a numerical model for predicting the behaviour of industrial thermal insulation and to compare model predictions and previous experimental results of small-scale fire tests (Bjørge et al., 2017, 2018). The model is also applied to systems that include a layer of more heat-resistant insulation, PFP, to see if that can prevent or delay breakdown of the insulation. Results are presented for 16-mm, 12-mm, 6-mm and 3-mm steel thicknesses (carbon steel), protected with a 50-mm layer of thermal insulation alone, as well as with an additional layer of 10 or 25 mm of PFP.

The materials and methods used in the study are outlined in Section 2. Section 3 presents the results from the numerical model. Section 4 presents the discussions and suggestions for future studies, and Section 5 offers the overall conclusions.

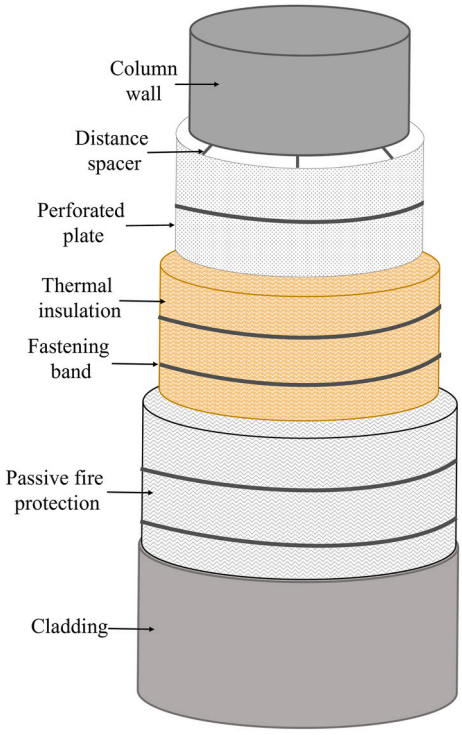

Fig. 1. Sketch of the current thermal insulation and passive fire protection methodology for corrosion prevention for a typical distillation column (Equinor, 2019).

2. Materials and methods

2.1. The thermal insulation studied

The thermal insulation used in the present study was 50-mm Rockwool (ProRox PSM 971). This insulation is used in several installations in the Norwegian oil and gas industry. The technical data and thermal conductivity up to 350 °C provided by the manufacturer is presented by Bjørge et al. (2018). The insulation is certified by the manufacturer for a maximum operating temperature of 700 °C. Data for higher temperatures are provided in other studies (Bjørge et al., 2017, 2018; Gunnarshaug et al., 2020). The insulation consists of several inorganic oxides, where the main components are: silica, magnesia, calcium oxide and iron (III) oxide, alumina and minor amounts of sodium oxide, titanium oxide, phosphorous pentoxide and potassium oxide. During production, the raw materials are melted at temperatures of up to 1500 °C; this is followed by spinning and cooling, and finally the insulation is cut to the desired size (Rockwool, 2023).

The spun and cooled fibres are individually woven to the final mat, resulting in high porosity, beneficial for the thermal insulation properties. The nominal density of the insulation is 140 kg/m^3 and bearing in mind the fact that the inorganic salts from which the insulation is made have densities that are about 20 times this value (silicon dioxide and aluminium oxide have densities of 2650 and 3950 kg/m^3, respectively), the porosity volume fraction is about 95%. This results in very low thermal conductivity at ambient conditions.

However, the maximum operating temperature of the insulation is 700 °C, hence when exposed to temperatures above this, the insulation starts to sinter and shrink (Bjørge et al., 2018; Gunnarshaug et al., 2020). This increases the thermal conductivity. Thermal conductivity of heat-treated thermal insulation samples was studied by Gunnarshaug et al. (2020, 2021), see Fig. 4. The thermal conductivity was found from TPS (Transient Plane Source) measurements. The TPS method has a ±2%–5% accuracy at ambient temperatures and at elevated temperatures ±5%–7% (ISO, 2015). The results are further adjusted with the shrinking of the thermal insulation during heating, adding an additional uncertainty to the effective thermal conductivity. A total of ±10% uncertainty is estimated for Equations (1)–(4) (Gunnarshaug et al., 2021).

The correlations for the effective thermal conductivity of the thermal insulation, k_{eff}, in Fig. 4 are:

$$k_{eff,T\leq 700\,°C} = 0.0304 + 3.111\cdot 10^{-10}T^3 \quad (1)$$

$$k_{eff,700\,°C<T\leq 1100\,°C} = 0.181 + 1.254\cdot 10^{-4}T \quad (2)$$

$$k_{eff,1100<T\leq 1200\,°C} = 0.354 + 1.0843\cdot 10^{-8}\cdot(T - 1373.15)^4 \quad (3)$$

$$k_{eff,T>1200\,°C} = 1.418 + 1.333\cdot 10^{-5}T \quad (4)$$

where T is the temperature in K.

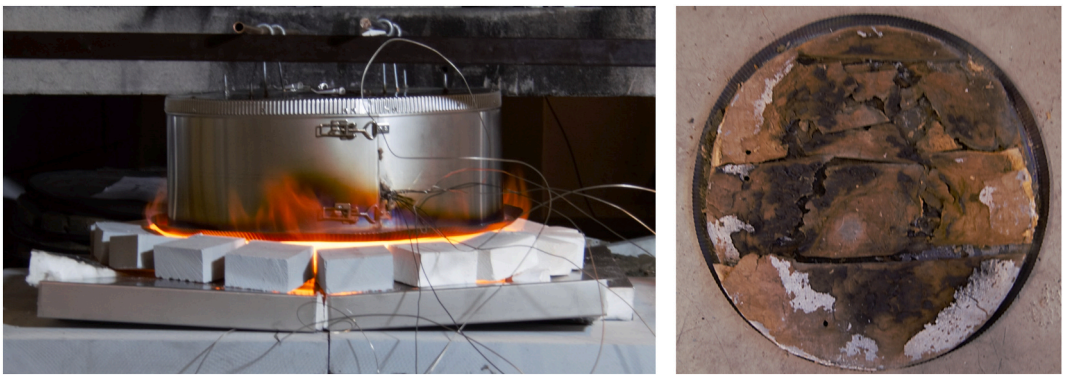

Fig. 2. Small-scale fire test (left) and thermal insulation after exposure to severe heat load (Bjørge et al., 2017, 2018).

Fig. 3. Thermal insulation samples after heat treatment in a muffle furnace to (a) virgin sample, (b) 700 °C, (c) 1000 °C, (d) 1180 °C, and (e) 1200 °C (adapted from Gunnarshaug et al., 2021).

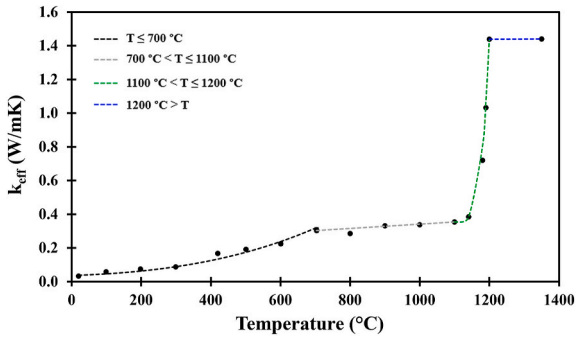

Fig. 4. Thermal conductivity as a function of heat treatment temperature, presented by Equations (1)–(4) (Gunnarshaug et al., 2021).

2.2. Activation energy of thermal insulation breakdown

Results from differential scanning calorimetry (DSC) analysis of the thermal insulation performed from ambient temperature to 1250 °C, at 5, 10, 20 and 40 K/min heating rates, are presented in Fig. 5. In both the DSC tests and the muffle oven tests, an exothermic reaction occurred between 800 and 900 °C (Bjørge et al., 2018; Gunnarshaug et al., 2020), followed by an endothermic peak at, or just above, 900 °C.

This indicates that energy is released inside the insulation, i.e., heat is generated, most likely due to (re)crystallization. It must be verified whether this heat generation will influence the temperature development in the numerical model. To account for this heat generation with varying heating rates in heat-exposed thermal insulation, the associated activation energy (E_a) and crystallization energy (E_c) had to be determined in the present study.

To find the activation energy (E_a), the non-isothermal method, described as the Ozawa plot (Ozawa, 1971), expressed by Equation (5), can be used.

$$\ln \alpha = -\frac{E_a}{R}\frac{1}{T_p} + C_1 \tag{5}$$

where α, E_a, R, T_p and $B1$ are the heating rate (K/min), activation energy (J/mol), ideal gas constant (8.314 J/(mol·K)), absolute peak temperature from the DSC curve (K), and a constant (−), respectively. The plot of ln α versus $1/T_p$ is expected to be linear, and the activation energy, E_a, can then be found from this plot. There are several similar methods for predicting the activation energy, e.g., by using the Kissinger method

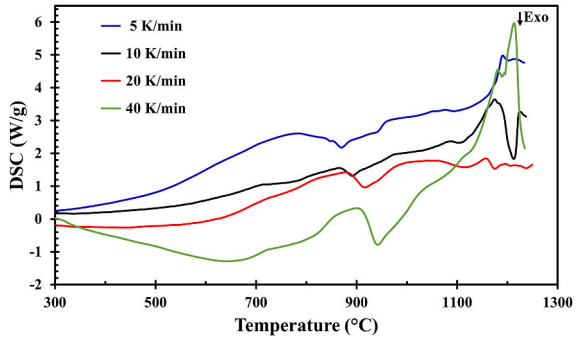

Fig. 5. DSC results as a function of temperature (adapted from Gunnarshaug et al., 2020).

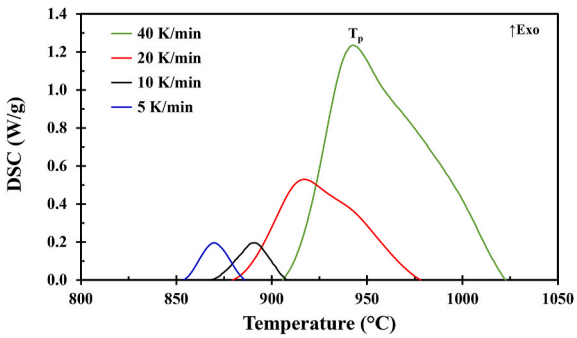

Fig. 6. DSC curve, exothermic reaction from Fig. 5.

(Kissinger, 1956) or the Matusita method (Matusita and Sakka, 1980).

The area under each curve presented in Fig. 6 represents the released heat during the exothermic reaction, i.e., the crystallization energy, E_c. Values for the peak temperature, T_p, for each curve are presented in Table 1. The plot of ln α versus $1/T_p$ for the different heating rates is presented in Fig. 7.

From the linear plot, an equation $y = ax + b$ can be derived (Equation (6)). From Equation (6), the variables can be defined by Equations (7)–(10), and the activation energy can be calculated by rearranging Equation (5). The calculated activation energy, E_a, and the constant, C, are presented in Table 2.

$$y = 3.9653 \cdot 10^4 x + 32.2 \tag{6}$$

$$y = \ln(\alpha) \tag{7}$$

$$x = \frac{1}{T_p} \tag{8}$$

$$a = -\frac{E_a}{R} \tag{9}$$

$$b = C_1 \tag{10}$$

In order to account for the crystallization energy, E_c, and the activation energy, E_a, in the numerical model, the Arrhenius expression for the rate coefficient is used (Drysdale, 2011), expressed by Equation (11).

$$k' = A \exp\left(-\frac{E_a}{RT}\right) \tag{11}$$

where A, E_a, R and T are the pre-exponential factor (constant), activation energy, ideal gas constant and the temperature in K, respectively.

The crystallization energy, E_c, found from the area under the exothermic peak, was simulated as closely as possible to reflect the DSC curve, shown in Fig. 8, using Equation (12). The E_c value from the DSC test with a heating rate of 40 K/min is used in the numerical model, since this is closest to heating rates observed in the fire tests. This was conservative, as it gave the highest energy release. The exponential factor A was chosen to be $2 \bullet 10^{12}$ s^{-1} to fit the DSC curve as closely as possible. The produced heat was calculated by Equation (12), until the crystallization energy, E_c, was consumed.

$$Q_{\text{prod,insu}} = k' E_c \Delta t \tag{12}$$

where E_c is expressed by Equation (13), and Δt is the numerical integration time step.

$$E_c = \text{previous } E_c - \text{Previous } Q_{\text{prod,insu}} \tag{13}$$

2.3. The passive fire protection studied

In the present study, high temperature fire protection (FyreWrap LT blanket, 50 mm, 128 kgm^{-3}, Unifrax) was studied as a representative PFP used in the Norwegian oil and gas industry. This PFP blanket is specifically designed for fire protection applications and certified for temperatures above 1200 °C. It consists solely of inorganic fibres, i.e., it does contain binder materials. When exposed to heat, it does not generate smoke. The main component in the PFP blanket is AES (Alkaline Earth Silicate) fibres, of which the main components are SiO_2, CaO and MgO (Unifrax, 2017). The detailed technical data and the thermal conductivity of the PFP are presented in Appendix A, Table A1 and A2.

Table 1
Peak temperature, T_p, for the different heating rates, α, from the DSC curve and the corresponding activation energy, E_c.

Heating Rate (K/min)	Heating Rate (K/s)	T_p (K)	$1/T_p$ (K^{-1})	ln(α) (−)	E_c (J/kg)
5	0.0833	1143	0.0008749	2.4849	39 884
10	0.1667	1165	0.0008584	1.7918	23 219
20	0.3333	1189	0.0008408	1.0986	81 847
40	0.6667	1216	0.0008225	0.4055	112 072

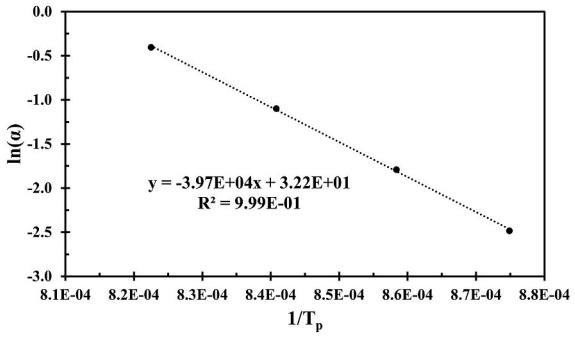

Fig. 7. Plot of ln α versus $1/T_p$ for the test samples of Rockwool thermal insulation (least squares method applied for the curve fitting).

Table 2
Activation energy, E_a, calculated from Equation (5) and constant, C, from Equation (10).

E_a (J/mol)	C
329 675	32.2

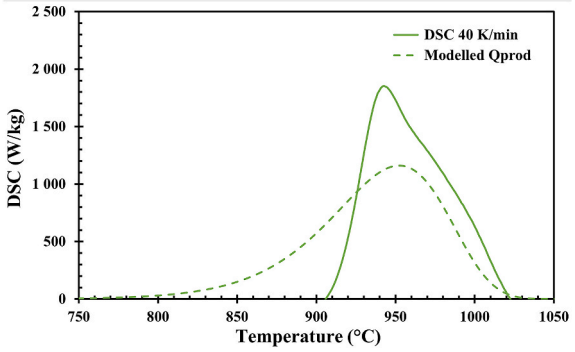

Fig. 8. Plot of the DSC curve with heating rate of 40 K/min and the calculated heat production used in the numerical model (dotted line).

In highly porous materials, the thermal conductivity is limited by pore radiation at ambient temperatures. For the thermal insulation, it is demonstrated by Bjørge et al. (2018) and Gunnarshaug et al. (2020) that the thermal conductivity will be proportional to the absolute temperatures to the third power. Similarly, the thermal conductivity can be expressed by Equation (14) for the PFP with density of 128 kg/m^3.

$$k_{pfp} = 7.0821 \cdot 10^{-11} T^3 + 5.311 \cdot 10^{-8} T^2 + 8.642 \cdot 10^{-6} T + 0.0438 \tag{14}$$

where T is the temperature in K.

The thermal conductivity for PFP with densities of 64 kg/m^3, 96 kg/m^3 and 128 kg/m^3, as a function of temperature, is presented in Fig. 9.

2.4. The numerical model

The fire exposure in the model is based on the measured temperatures in previous small-scale jet fire tests by Bjørge et al. (2017, 2018) presented in Fig. 2.

In the process industry, 0.7-mm stainless steel cladding is used as weather protection. In the numerical model, shown in Fig. 10, this layer

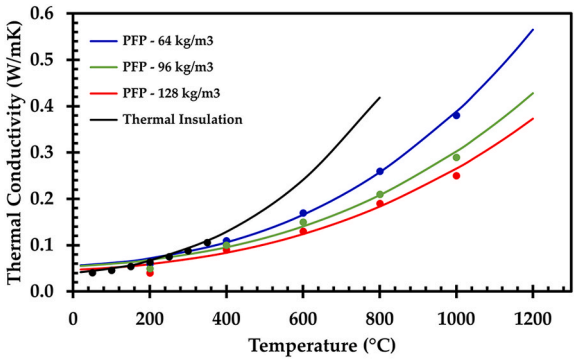

Fig. 9. Thermal conductivity of the thermal insulation (Gunnarshaug et al., 2020) and passive fire protection with density of 64 kg/m^3, 96 kg/m^3 and 128 kg/m^3 (data from Appendix A).

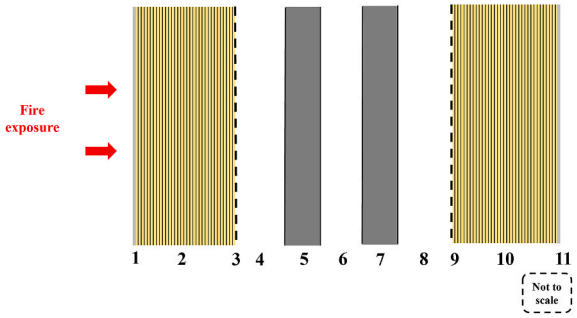

Fig. 10. Sketch of the fire exposure model. Weather protection cladding (1), thermal insulation (2), perforated steel plate (3), air gap (4), the exposed steel member (5), air gap (6), unexposed steel member (7), air gap (8), unexposed perforated plate (9), unexposed thermal insulation (10), unexposed cladding (11).

is marked as layer 1. The typically 50 mm thick thermal insulation layer (layer 2) is divided into 25 sheets, and the temperature is calculated from the weather cladding (layer 1), through the thermal insulation, perforated plate and, further, through the exposed and unexposed steel members. The thermal insulation and cladding on the unexposed side are also included in the model to mimic in the best possible way the mock-up used for fire testing. This setup resembles process equipment, for simplicity, compressed to a near flat structure. The build-up of the calculated configuration, with a base in the same setup as in the small-scale fire tests (Bjørge et al., 2017, 2018), is presented in Fig. 10. The unexposed side, layers 8 to 11, was included to replicate the set-up of the small-scale testing as close as possible. The modelling was completed by calculating temperatures in the layers and integration with time.

The cladding and perforated plates were made of stainless steel, while the exposed and unexposed steel plates were made of carbon steel. The thermal insulation was 50-mm Rockwool (ProRox PSM 971, 50 mm, Rockwool). The heat transfer through the different layers is based on general heat transfer equations, presented by Equations (15)–(18).

The heat in and heat out are calculated for each layer, considering proper boundary conditions, temperature-dependent parameters, etc. The fire exposure in the model is based on the measured plate thermocouple temperature recorded in the small-scale fire tests (Bjørge et al., 2017, 2018). Through the insulation layers, conduction and convection are accounted for. As the thermal insulation starts to sinter and make air gaps, radiation is also included in the model. Through the air gaps, there are radiation and convection. Steel member dimensions and thermal properties, versus the thermal insulation dimension and properties, allowed the steel members to be treated as lumped heat transfer bodies.

The heat transfer through the insulation layers is governed by heat conduction, which may be presented by Fourier's law, given by Equation (15).

$$\dot{q}''_{cond} = -k\nabla T \left(\frac{W}{m^2}\right), \tag{15}$$

where k is the thermal conductivity (W/(m·K)), and ∇ is the temperature gradient (K/m). The material properties, i.e., the thermal conductivity, density, and heat capacity of the thermal insulation, will change as a function of temperature and are expressed by Equation (16).

$$\frac{dT}{dt} = \frac{d}{dx}\left(\frac{k}{\rho c_p}\right)\frac{dT}{dx} \tag{16}$$

where ρ is the density (kg/m^3) and c_p is the specific heat capacity (J/(kg·K)).

The internal convection through the insulation and through the airgaps may be expressed by Equation (17).

$$\dot{q}''_{conv} = h\Delta T \left(\frac{W}{m^2}\right), \tag{17}$$

where h is the convective heat transfer coefficient (W/(m^2·K)) and ΔT is the temperature difference (K).

The radiative heat transfer through the perforated plate, between the steel plates (air gap) and, after severe heat exposure, through the sintered insulation layers, is expressed by Equation (18).

$$\dot{q}''_{rad} = \varepsilon\sigma\left(T^4_{cladd} - T^4_n\right)\left(\frac{W}{m^2}\right), \tag{18}$$

where ε is the emissivity (W/(m^2·K^4)), σ is the Stefan–Boltzmann constant, T_{cladd} is the cladding temperature (K) and T_n is the temperature (K) in the current layer.

All equations used in the numerical model are presented in detail in Appendix B. All the constants used in the numerical model are presented in Table 3. The thermal conductivity of the thermal insulation was, however, expected to vary much with increasing temperature. It was also expected to change significantly on the significant sintering and

Table 3
Constants used in the numerical model.

Constant	Symbol	Value	Unit
Thermal insulation thickness	L_i	0.05	m
Passive fire protection thickness	L_{pfp}	0.01	m
Time step	Δt	0.1	s
Length step, thermal insulation	Δx	$\frac{L_i}{25}$	m
Length step, passive fire protection	Δx_{pfp}	$\frac{L_{pfp}}{5}$	m
Cladding thickness	L_{kap}	0.0007	m
Perforated plate thickness	L_{perf}	0.00059	m
Steel plate thickness	L_{steel}	0.016	m
		0.012	m
		0.006	m
		0.003	m
Heat transfer coefficient	h_s	10	W/(m^2·K)
Heat transfer coefficient	h_f	100	W/(m^2·K)
Heat transfer coefficient	h_{insu}	4[a]	W/(m^2·K)
Density thermal insulation	ρ_{insu}	140	kg/m^3
Density passive fire protection	ρ_{pfp}	128	kg/m^3
Density steel	ρ_{steel}	7700	kg/m^3
Stefan Boltzmann constant	σ	5.67E8	W/(m^2·K^4)
Emissivity	ε	0.85	–
Initial temperature	T_{init}	15	°C
Open fraction	O_f	0.32	–
Closed fraction	C_f	0.68	–
Preexponential factor	A	2E12	s^{-1}
Activation energy	E_a	329 675	J/mol
Ideal gas constant	R_g	8.314	J/(mol·K)
Crystallization energy	E_c	112 070	J/kg

[a] Found by trial.

partial melting of the thermal insulation.

2.5. Additional layer of PFP

The numerical model was also tested with an extra layer of PFP, i.e., 50 mm thermal insulation + a layer of PFP, where the same principle was used. A 10-mm and a 25-mm layer of PFP were added in the model, similarly to the thermal insulation layer but without any degradation mechanisms in the PFP layer, as presented in Fig. 11. The modelling was completed by calculating temperatures in the layers and integration with time.

3. Results

3.1. Thermal insulation

The modelled temperature in the exposed and unexposed carbon-steel plate as a function of time, compared to the recorded steel plate temperatures during the small-scale high temperature fire testing, with 16-mm carbon-steel plate thickness, is presented in Fig. 12. The cladding temperature used in the model is based on the measured cladding temperature during the small-scale testing.

The modelled thermal insulation temperature is presented as a function of time in Fig. 13.

The modelled temperature in the exposed and unexposed carbon-steel plate as a function of time compared to the recorded carbon-steel plate temperatures during the small-scale high temperature fire testing, with 12-mm steel plate thickness, is presented in Fig. 14.

A value of $h = 4$ W/(m^2·K) seems to give the best fit with the small-scale test results, as shown in Fig. 12. It should, however, be mentioned that the temperature time curve from the small-scale fire tests is an average of several tests, and that there were, as expected, some variations in recorded temperatures in the small-scale testing.

In the small-scale fire testing by Bjørge et al. (2017, 2018), the small-scale mock-up was heated from below, i.e., there will be convection through the insulation layer. The convection is accounted for in the model; however, no literature supporting the selection of the internal convective heat transfer coefficient, h, for the insulation was identified. The value of h was therefore obtained by trial and error; the modelled exposed carbon-steel plate temperature as a function of time with different values of h is presented in Fig. 15. For the calculation, the convective heat transfer coefficient was chosen to be 4 W/(m^2·K) for the 16-mm and 12-mm steel plate thicknesses, as this gave the best fit compared to the results from the small-scale testing. To be conservative, h = 6 W/(m^2·K) is, however, recommended for engineering calculations.

The modelled temperature in the exposed and unexposed carbon-steel plate as a function of time, compared to the recorded carbon-steel plate temperatures during the small-scale high temperature fire testing, with 6-mm steel plate thickness, is presented in Fig. 16. A convective heat transfer coefficient of 4 does not seem to be valid for the thinner steel plates, i.e., 6-mm and 3-mm steel plate thicknesses, as shown in Fig. 16. Decreasing the convective heat transfer coefficient to 1 for the thinner steel plates gave a better fit with the small-scale fire tests for the thinner steel plates, as presented in Figs. 17 and 18. However, the temperature in the unexposed steel plate is still overestimated.

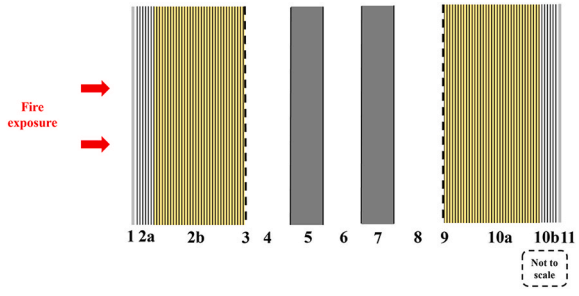

Fig. 11. Sketch of the fire exposure model. Weather protection cladding (1), passive fire protection insulation (2a), thermal insulation (2b), perforated steel plate (3), air gap (4), the exposed steel (5), air gap (6), unexposed steel (7), air gap (8), unexposed perforated plate (9), unexposed thermal insulation (10a), unexposed passive fire protection (10b), unexposed cladding (11).

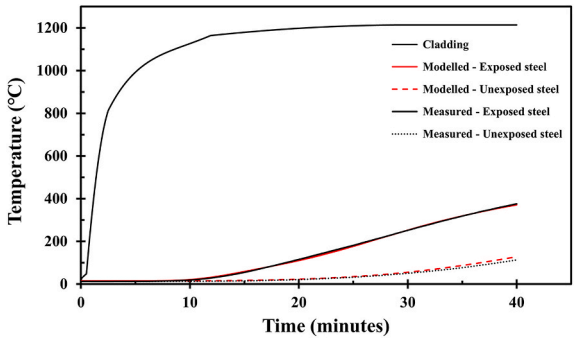

Fig. 12. Temperature measurements during small-scale jet fire tests performed by Bjørge et al. (2017, 2018) and modelled temperature in the exposed and unexposed steel, when a 16-mm steel plate is protected with 50-mm thermal insulation (convective heat transfer coefficient of $h = 4$ W/(m^2·K) for the thermal insulation).

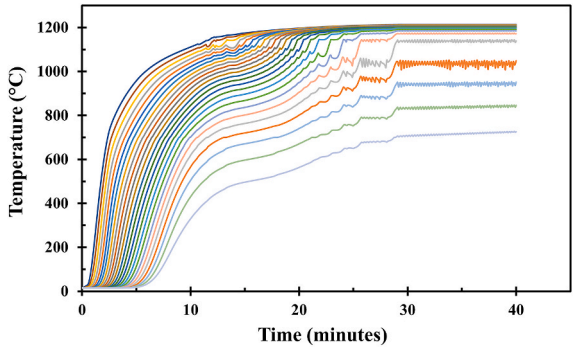

Fig. 13. Modelled temperature through the 25 layers of thermal insulation as a function of time, for carbon-steel plate thickness of 16 mm.

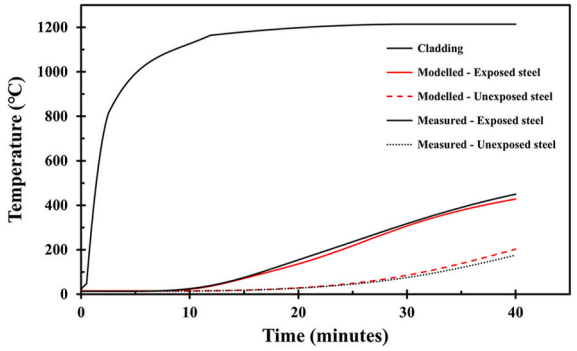

Fig. 14. Temperature measurements during small-scale jet fire tests performed by Bjørge et al. (2017, 2018), black curves, and modelled temperatures in the exposed and unexposed carbon-steel, when a 12-mm steel plate is protected with 50-mm thermal insulation (convective heat transfer coefficient of $h = 4$ W/(m^2·K) for the thermal insulation).

3.2. Thermal insulation and passive fire protection

As demonstrated by Bjørge et al. (2018) and Gunnarshaug et al.

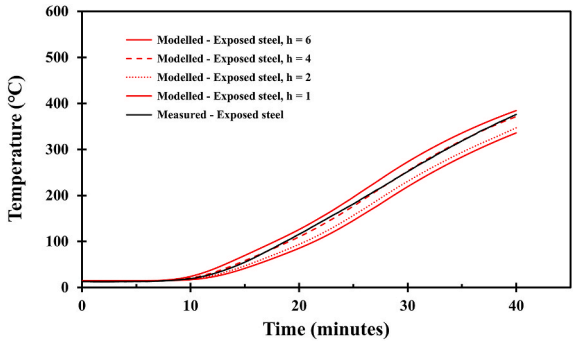

Fig. 15. Temperature measurements during small-scale jet fire tests performed by Bjørge et al. (2017, 2018) vs modelled temperature in the exposed and unexposed steel, for a 16-mm steel plate protected with 50-mm thermal insulation, comparison with different values for the convective heat transfer coefficient, h, for the thermal insulation.

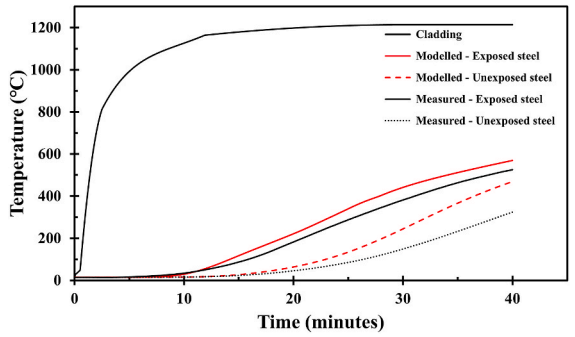

Fig. 16. Temperature measurements during small-scale jet fire tests performed by Bjørge et al. (2017, 2018) and modelled temperature in the exposed and unexposed steel, when a 6-mm steel plate is protected with 50-mm thermal insulation (convective heat transfer coefficient of $h = 4$ W/(m^2·K) for the thermal insulation).

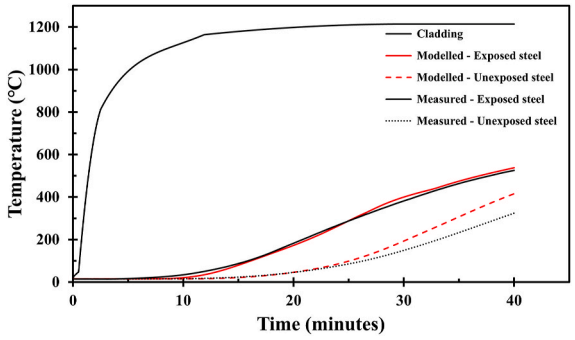

Fig. 17. Temperature measurements during small-scale jet fire tests performed by Bjørge et al. (2017, 2018) vs modelled temperature in the exposed and unexposed carbon-steel, when a 6-mm steel plate is protected with 50-mm thermal insulation (convective heat transfer coefficient of $h = 1$ W/(m^2·K) for the thermal insulation).

(2020), when the thermal insulation is exposed to high temperatures, the insulation starts to sinter. Upon further heating, significant shrinking and cracking of the insulation occur, especially at temperatures above 1100 °C. It is therefore interesting to see how a thin layer of more heat-resistant insulation, i.e., passive fire protection, can protect the thermal insulation from the highest temperatures and thus prevent the breakdown. Therefore, a 10-mm layer of PFP was added in the model, similarly to the thermal insulation layer but without the degradation

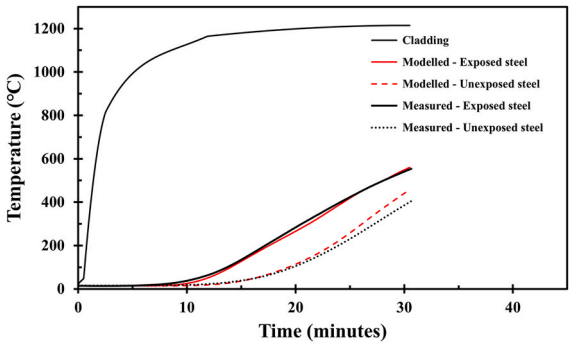

Fig. 18. Temperature measurements during small-scale jet fire tests performed by Bjørge et al. (2017, 2018) vs modelled temperature in the exposed and unexposed steel, when a 3-mm steel plate is protected with 50-mm thermal insulation (convective heat transfer coefficient of $h = 1$ W/(m^2·K) for the thermal insulation).

mechanisms. The modelled temperature as a function of time for the 16-mm-thick carbon-steel plates, with an extra layer of 10-mm PFP or 25-mm PFP, is compared to the measured temperature during the small-scale fire tests with thermal insulation, in Fig. 19.

The temperature development through the 10-mm PFP (stippled lines) and 50-mm thermal insulation as a function of time for the 16-mm carbon-steel plate is presented in Fig. 20. The temperature development for the 25-mm PFP is similarly presented in Fig. 21.

It is clearly seen from Fig. 19 that the 10-mm-thick layer of PFP significantly reduced the temperature increase in the exposed steel member. The improvement achieved by, rather, adding a 25-mm-thick PFP layer does not result in much further increase in heat protection. This may possibly be explained by looking at the details of Fig. 20, where it is seen that the 10-mm-thick PFP helps protect the most exposed part of the thermal insulation, which does not exceed a temperature of 1100 °C. Thus, the thermal insulation to a great extent has been protected from reaching temperatures where it starts to deteriorate.

4. Discussion

Previous studies have shown that industrial thermal insulation to some extent may serve as passive fire protection, especially when the fire-exposed carbon-steel equipment itself represents a significant heat sink (Bjørge et al., 2017, 2018). Exposing the insulation to temperatures above the operating temperature, i.e., above 700 °C, sintering and loss of thickness occurs in the insulation material. Exposing the insulation to even higher temperatures, i.e., above 1100 °C, shrinking occurs in all dimensions. Muffle furnace tests have indicated that the thermal insulation has a breakdown temperature around 1200 °C (Gunnarshaug

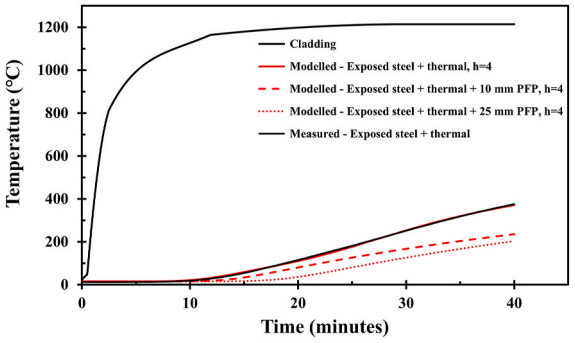

Fig. 19. Temperature measurements during small-scale fire tests performed by Bjørge et al. (2017, 2018) and modelled temperature in the exposed and unexposed steel, when a 16-mm steel plate is protected with only 50-mm thermal insulation and protected by an additional layer of 10-mm PFP or 25-mm PFP.

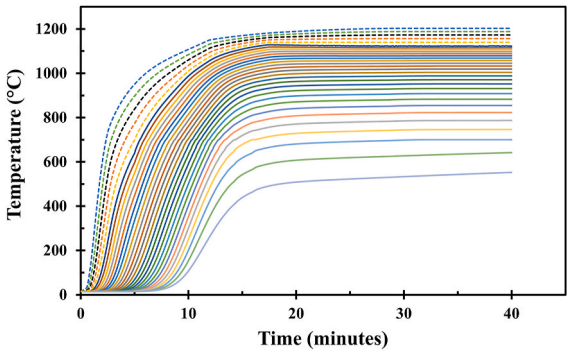

Fig. 20. Modelled temperature through the sheets of 10-mm-thick PFP (stippled lines) and the 50-mm-thick thermal insulation for steel plate thickness of 16 mm as a function of time.

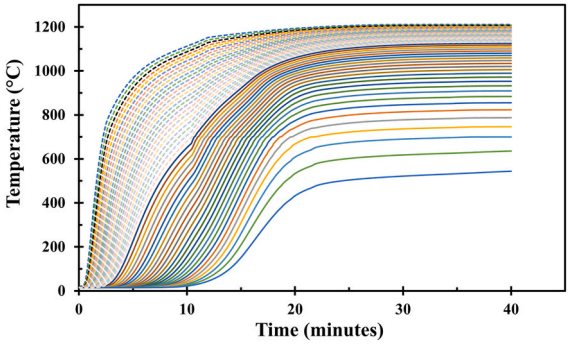

Fig. 21. Modelled temperature through the sheets of 25-mm-thick PFP (stippled lines) and the 50-mm-thick thermal insulation for steel plate thickness of 16 mm as a function of time.

et al., 2020, 2021). Keeping the temperature in the thermal insulation layer below 1100 °C, by adding a layer of more heat resistant insulation, i.e., PFP, would therefore prevent, or extend the time to, breakdown of the insulation. The objective of the present study was to create a numerical model, resembling the test set-up as shown in Fig. 2 by Bjørge et al. (2017, 2018), predicting the temperature development through the thermally insulated system. In addition, a layer of PFP was added in the model, to evaluate the possible increased performance of this combination.

The test conditions were based on a 4-m-diameter distillation column with an exposed side and an unexposed side, where the small-scale set-up is compacted for testing. Given a distillation column wall thickness to diameter ratio less than 1/100, the system could be seen as one dimensional. The numerical model resembling the test conditions was therefore also based on a one-dimensional system.

The properties of the thermal insulation when exposed to high temperatures were also accounted for in the numerical model.

The density was kept constant at 140 kg/m^3. As the thermal insulation started to crystallize and melt, it reached a more stone-like structure, i.e., the density of the thermal insulation increased with the increased temperature. However, the change in density is not significant before the temperature in the insulation reaches above 1150 °C. The effective thermal conductivity did, however, account for the change in thermal insulation dimensions, i.e., the density. At thermal insulation temperatures above 1150 °C, heat radiation through the cracks dominated the heat transfer through the thermal insulation.

Previous TGA/DSC at 5 K/min, 10 K/min, 20 K/min and 40 K/min and muffle furnace tests (Bjørge et al., 2018; Gunnarshaug et al., 2020) revealed an exothermic reaction at about 900 °C, most likely due to recrystallization. Whether it was necessary to include this in the numerical model was therefore investigated. To be conservative, the highest activation energy observed, i.e., at 40 K/min heating rate, was chosen to investigate whether this crystallization had any influence on the modelled temperature of the fire-exposed steel. It turned out that this recrystallization did not have any significant effect on the temperature development. Regardless of that, it was decided to keep it in the numerical model in case it should be required for other thermal insulation types in future modelling.

Accounting for all the mentioned thermal insulation properties, results from the numerical model were compared to the small-scale fire exposure measurements performed in previous studies for 16-mm, 12-mm, 6-mm and 3-mm steel plate thicknesses (Bjørge et al., 2017, 2018); see Figs. 12 and 14 for the 16-mm and 12-mm carbon-steel plate, respectively. There is a small overestimation of the temperature in the unexposed carbon-steel plate, most visible for plate thickness of 12 mm. Small variations were observed in the different tests, as reported by Bjørge et al. (2018), and it should be kept in mind that the results from the experimental testing represent an average from three experiments, regarding both cladding temperature and the temperature measured in the exposed and unexposed carbon-steel members. It may generally be concluded that the modelled results fit quite well with previous fire testing.

The numerical model displayed temperature instability in the thermal insulation layers when the cladding temperature stabilized at about 1200 °C, as presented in Fig. 13. This may be explained by the significant cracking and shrinking of the insulation occurring at temperatures above 1100 °C. As seen in Fig. 13, sheet 21 of the thermal insulation in the model is, at just around 1100 °C, on the verge of breaking down, probably causing the instability in layers 21 to 25 of the insulation. Smaller time steps were tested, down to 0.005 s, but no significant change in the stability of the modelled temperatures was observed.

During fire testing, as shown in Fig. 2, the heat exposure was vertically upwards. This testing would also lead to contribution in heat transfer by convection. As no literature data were revealed regarding the convective contribution, the convective heat transfer coefficient, h_i, was determined by trial and error, as shown in Fig. 15. The heat transfer coefficient should have been a function of temperature, but the authors had no method for estimating the temperature dependency. A factor of 4 W/(m^2·K) was found to give a good fit with the experimental results. To be conservative, a factor of 6 W/(m^2·K) is recommended for engineering calculations.

Using a convective heat transfer coefficient of 4 W/(m^2·K) results in too high temperatures for the thinner steel plates, compared to the experimental fire test results, as shown in Fig. 16. A convective heat transfer coefficient of 1 W/(m^2·K) in the insulation layers gave a better fit for the thinner steel plates, as shown in Figs. 17 and 18. The authors have no good explanation for this observation. The overestimation of the temperature in the unexposed carbon-steel plate is also more visible for the 3-mm and 6-mm steel members than for the thicker ones.

The previous insulation method typically included a 50-mm layer of thermal insulation, for heat or cold conservation, in contact with the steel member to be protected, on top of which an additional layer of 50-mm PFP was mounted. The new insulation method includes a 25-mm air gap between the steel surface and the thermal insulation. In an existing process plant, with piping, structures and other equipment in near proximity, there may not be room for a 50-mm increase in diameter without extensive construction work. However, there may still be room for a thinner layer of PFP, e.g., 25-mm or 10-mm thickness. It was therefore interesting to see whether adding a thin layer of PFP to the numerical model would at least theoretically protect the thermal insulation from the dimensional changes and melting, by keeping its temperature below 1100 °C.

The passive fire protection used in the model is certified for temperatures above 1200 °C, i.e., no breakdown or dimensional changes are expected to occur in the fire exposure conditions considered in the present study. This should, however, be confirmed by similar small scale fire tests and muffle furnace tests to those conducted by Bjørge et al.

(2018) and Gunnarshaug et al. (2020), for the thermal insulation, including an additional PFP layer of, e.g., 10 mm or 25 mm. Pore heat radiation is expected to dominate the heat transfer through the entire fire exposure for this PFP layer.

During the first 20 min of the numerical modelling, no significant difference was observed between the temperature of the carbon steel protected with only thermal insulation or that of the two modelled cases with an extra layer of 10-mm PFP and 25-mm PFP. However, while the breakdown of the thermal insulation starts to dominate in the cases without PFP, the steel member temperature in the cases with PFP increased less and thereby significantly extended the time until the thermal insulation reached 1100 °C, as shown in Fig. 19. This can also be seen in the temperature development in the insulation layers, presented in Fig. 20, where 16-mm steel is protected with a layer of 50-mm thermal insulation in addition to 10-mm PFP. The temperature of the most exposed part of the thermal insulation stabilizes just above 1100 °C, i.e., no significant changes in the thermal insulation properties occur. Adding a thicker layer of PFP of 25 mm further delayed the time to temperature increase in the carbon-steel plate. For the carbon-steel plate protected with 50-mm thermal insulation alone, the plate-temperature increase started after about 10 min of exposure. Adding a layer of 25-mm PFP extends this time to 17 min. After 40 min, the temperature in the exposed carbon-steel plate was approximately 370 °C. Adding a layer of 10 mm or 25 mm of PFP reduced the temperature to 235 °C and 202 °C, respectively, after 40 min. It may then be concluded that even a 10-mm layer of PFP significantly extends the lifetime of the thermal insulation during fire exposure, by preventing the temperature of the most exposed part of the thermal insulation from entering the regime of significant thermal breakdown.

When a 25-mm layer of PFP was added, the temperature in the most exposed part of the thermal insulation stabilized just above 1100 °C, as shown in Fig. 21, while the remaining thermal insulation was kept at temperatures below this level, i.e., the breakdown of the thermal insulation would be expected to be very limited. Future research should verify the actual effect of adding a layer of PFP of, e.g., 10 mm or 25 mm, through similar small-scale testing as that in Bjørge et al. (2017, 2018) and possibly for full-scale jet fire testing. Such verification was outside the scope of the present work.

5. Conclusions

The presented numerical model including thermal insulation breakdown gives a good indication of the temperature development for thermally insulated 16-mm-, 12-mm-, 6-mm- and 3-mm-thick steel plates exposed to fire, as previously experimentally tested. There are some uncertainties regarding the internal convective heat transfer coefficient in the insulation layers giving conservative results, especially for thin steel plates. The numerical modelling indicates that adding a 10-mm layer of PFP will significantly extend the time to breakdown of the thermal insulation. It is, however, recommended that this be confirmed by fire testing. The model can easily be adjusted to radial coordinates, allowing for modelling fire exposure of smaller equipment, e.g., piping and valves.

Credit author statement

Amalie Gunnarshaug: Software, Validation, Formal analysis, Investigation, Writing – original draft. **Torgrim Log**: Conceptualization, Methodology, Formal analysis, Investigation, Writing – review & editing, Supervision. **Maria-Monika Metallinou**: Formal analysis, Investigation, Writing – review & editing, Supervision, Funding acquisition. **Trygve Skjold**: Writing – review & editing, Supervision.

Funding

A.G. was supported by Gassco AS, Norway, and the Norwegian Research Council, Grant No. 305336.

Declaration of competing interest

The authors declare the following financial interests/personal relationships which may be considered as potential competing interests: Amalie Gunnarshaug reports financial support was provided by Gassco AS.

Data availability

Data will be made available on request.

Acknowledgments

The authors would like to acknowledge technical support with the Python coding from Even Kallevik.

Appendix A

The technical data for the passive fire protection (PFP) are given in Tables A1 and A2.

Table A1
Technical data for the FyreWrap LT Blanket passive fire protection (Unifrax, 2017).

	Description	
Material	FireMaster Marine Plus Blanket	
	Performance	**Norms**
Maximum service temperature	>1200 °C	
Reaction to fire	Non-Combustible A1	IMO FTP code Part 1 EN 13501-1
Nominal density	128 kg/m^3	

Table A2
Thermal conductivity of the FyreWrap LT Blanket, 128 kg/m^3 (Unifrax, 2017).

Temperature (°C)	Thermal conductivity 64 kg/m^3 (W/(m·K))	Thermal conductivity 96 kg/m^3 (W/(m·K))	Thermal conductivity 128 kg/m^3 (W/(m·K))
200	0.06	0.06	0.05
400	0.11	0.09	0.08
600	0.17	0.14	0.12
800	0.26	0.20	0.18
1000	0.38	0.29	0.25

Appendix B

The fire exposure in the model is based on the measured plate thermocouple temperature recorded in the small-scale fire tests (Bjørge et al., 2017, 2018) and is predicted by Equations B.1 to B.5. The heat transfer through the different layers is calculated by Equations B.6 to B.16, based on general heat transfer equations. Abbreviations used in Equations B.1 to B.26 are described in Table B1.

Table B1
Abbreviations used in Equations B.1 to B.26.

Description	Symbol	Unit
Cladding temperature	T_{cladd}	°C
Time	t	s
Effective heat transfer coefficient, cladding	h_{eff}	W/(m^2·K)
Length step	dx	m
Thermal conductivity of the thermal insulation	k_{insu}	W/(m·K)
Heat transfer coefficient of the thermal insulation	h_{insu}	W/(m^2·K)
Radiated heat through the insulation layers	Q_{rad}	W
Time step	Δt	s
Density of the thermal insulation	ρ_{insu}	kg/m^3
Heat capacity of the insulation	$C_{p,insu,T\_i}$	J/(kg·K)
Produced heat in the thermal insulation	$Q_{prod,\ insu}$	W
Closed fraction perforated plate	C_f	–
Inverse of closed fraction perforated plate	$InvC_f$	–
Open fraction perforated plate	O_f	–
Inverse of open fraction perforated plate	$InvO_f$	–
Thickness perforated plate	l_{perf}	m
Heat capacity of carbon steel	$C_{p,cs}$	J/(kg·K)
Thickness steel plate	l_s	m
Heat transfer coefficient steel	h_s	W/(m^2·K)

The heat transfer from the fire to the exposed object, where the first layer is the cladding, is expressed by Equations B.1 to B.5, representing the measured cladding temperature (radiated heat from the fire to the cladding) during the small-scale testing in Bjørge et al. (2017 and 2018). This corresponds to layer n = 0 in the numerical model. The calculated temperatures and input temperatures in Equations B.1 to B.26 are in K.

If t < 30 s

$$T_{cladd} = 1.268t + 293.53 \tag{B.1}$$

If 30 s ≤ t < 150 s:

$$T_{cladd} = -3.183E-02t^2 + 12.126t - 18.242 \tag{B.2}$$

If 150 s ≤ t < 712 s:

$$T_{cladd} = -9.502\cdot10^{-9}t^4 + 1.835\cdot10^{-5}t^3 - 1.358\cdot10^{-2}t^2 + 4.981t + 580.157 \tag{B.3}$$

If 712 s ≤ t < 1756 s:

$$T_{cladd} = -4.283\cdot10^{-5}t^2 + 0.1467t + 1353.037 \tag{B.4}$$

If t ≥ 1756 s:

$$T_{cladd} = 1487.3 \tag{B.5}$$

The calculated temperature in the first insulation layer is expressed by Equation B.6.

$$T_{ci,i,t+\Delta t,n=1} = T_{i,n} + \left(\left(\frac{T_{i-1,n-1} - T_{i,n}}{\frac{1}{h_{eff,T_{i-1,n-1},T_{i,n}}} + \frac{0.5\Delta x}{k_{insu,T_{i,n}}}} - \frac{T_{i,n} - T_{i+1,n+1}}{\frac{0.5\Delta x}{k_{insu,T_{i,n}}} + \frac{0.5\Delta x}{k_{insu,T_{i+1,n+1}}}} + h_{insu}\left(T_{i,n} - T_{i+1,n+1}\right) + \Delta Q_{rad,i,t+\Delta t} \right) \cdot \frac{\Delta t}{\rho_{insu} c_{p,insu,T_{i,n}} \Delta x} \right) + \frac{Q_{prod,insu}}{c_{p,insu,T_{i,n}}} \tag{B.6}$$

when both the previous and the next layer are thermal insulation, corresponding to layers 2 ≤ n ≤ 24 in the model, the calculated temperature is given by Equation B.7.

$$T_{i,t+\Delta t,2\le n\le 24} = T_{i,n} + \left(\left(\frac{T_{i-1,n-1} - T_{i,n}}{\frac{0.5dx}{k_{insu,T_{i-1,n-1}}} + \frac{0.5dx}{k_{insu,T_{i,n}}}} - \frac{T_i - T_{i+1}}{\frac{0.5dx}{k_{insu,T_{i,n}}} + \frac{0.5dx}{k_{insu,T_{i+1,n+1}}}} + h_{insu}\left(T_{i,n} - T_{i+1,n+1}\right) + \Delta Q_{rad,i,t+\Delta t} \right) \cdot \frac{dt}{\rho_{insu} c_{p,insu,T_{i,n}} \Delta x} \right) + \frac{Q_{prod,insu}}{c_{p,insu,T_{i,n}}} \tag{B.7}$$

The temperature in the last insulation layer, i.e., when the next layer is the perforated plate, corresponding to layer n = 25 in the model, is expressed by Equation B.8.

$$T_{iperf,i,t+\Delta t,n=25} = T_{i,n} + \left(\left(\frac{T_{i-1,n-1} - T_{i,n}}{\frac{0.5dx}{k_{insu,T_{i-1,n-1}}} + \frac{0.5dx}{k_{insu,T_{i,n}}}} - \frac{T_{i,n} - T_{i+1,n+1}}{\frac{0.5dx}{k_{insu,T_{i,n}}} + \frac{Inv_{C_f}}{h_{eff,T_i,T_{i+1}}}} - \frac{T_{i,n} - T_{i+2,n+2}}{\frac{0.5dx}{k_{insu,T_{i,n}}} + \frac{Inv_{O_f}}{h_{eff,T_i,T_{i+2}}}} + h_{insu}\left(T_{i-1,n-1} - T_{i,n}\right) + \Delta Q_{rad,T_{i-1},T_i,t} \right) \cdot \frac{dt}{\rho_{insu} c_{p,insu,T_{i,n}} \Delta x} \right) + \frac{Q_{prod,insu}}{c_{p,insu,T_{i,n}}} \tag{B.8}$$

The temperature in the perforated plate, corresponding to layer n = 26 in the model, is expressed by Equation B.9.

$$T_{perf,i,t+\Delta t,n=26} = T_{i,n} + \left(\frac{T_{i-1,n-1} + T_{i,n}}{\frac{Inv_{C_f}}{h_{eff,T_{i-1},T_i}} + \frac{0.5dx}{k_{insu,T_{i-1,n-1}}}} - \left(T_{i,n} - T_{i+1,n+1}\right) O_f h_{eff,T_i,T_{i+1}} \right) \cdot \frac{dt}{\rho_s c_{p,s,T_{i,n}} l_{perf}} \tag{B.9}$$

The temperature in the exposed steel plate, for layer n = 27 in the model, is expressed by Equation B.10.

$$T_{exp,i,t+\Delta t,n=27} = T_{i,n} + \left(\frac{T_{i-2,n-2} - T_{i,n}}{\frac{0.5dx}{k_{insu,T_{i-2,n-2}}} + \frac{Inv_{O_f}}{h_{eff,T_{i-2},T_i}}} + \left(T_{i-1,n-1} - T_{i,n}\right) O_f h_{eff,T_{i-1},T_i} - \left(T_{i,n} - T_{i+1,n+1}\right) h_{eff_{T_i,T_{i+1}}} \right) \cdot \frac{dt}{\rho_s c_{p,cs,T_{i,n}} l_s} \tag{B.10}$$

The temperature in the unexposed steel plate, for layer n = 33 in the model, is expressed by Equation B.11.

$$T_{unexp,i,t+\Delta t,n=28} = T_{i,n} + \left(\begin{array}{c} \left(\left(T_{i-1,n-1} - T_{i,n}\right) h_{eff_{Ti-1,T_i}} \right) + \left(\varepsilon\sigma\left(\left(T_{i,n-1}\right)^4 - \left(T_{i+1,n}\right)^4 \right) \right) - \left(\left(T_{i,n} - T_{i+1,n+1}\right) h_{eff_{Ti,T_{i+1}}} O_f \right) \\ - \frac{T_{i,n} - T_{i+2,n+2}}{\frac{Inv_{O_f}}{h_{eff,T_i,T_{i+2}}} + \frac{0.5dx}{k_{insu,T_{i+2,n+2}}}} - \left(\varepsilon\sigma\left(\left(T_{i,n+1}\right)^4 - \left(T_{i+1,n+2}\right)^4 \right) O_f \right) \end{array} \right) \cdot \frac{dt}{\rho_s c_{p,cs,T_{i,n}} l_s} \tag{B.11}$$

The temperature in the unexposed perforated plate, for layer n = 29 in the model, is expressed by Equation B.12.

$$T_{perfunexp,i,t+\Delta t,n=29} = T_{i,n} + \left(\left(\left(T_{i-1,n-1} - T_i\right) h_{eff_{Ti-1,T_i}} C_f \right) - \frac{T_{i,n} - T_{i+1,n+1}}{\frac{Inv_{C_f}}{h_{eff,T_i,T_{i+1}}} + \frac{0.5dx}{k_{insu,T_{i+1,n+1}}}} \right) \cdot \frac{dt}{\rho_s c_{p,s,T_{i,n}} l_{perf}} \tag{B.12}$$

The temperature in the first insulation layer on the unexposed side, i.e., when the next layer after the perforated plate is the insulation layer, for layer n = 30 in the model, is expressed by Equation B.13.

$$T_{perfiunexp,i,t+\Delta t,n=30} = T_{i,n} + \left(\frac{T_{i-2,n-2} - T_{i-1,n-1}}{\frac{Inv_{Cf}}{h_{eff,T_{i-2},T_{i-1}}} + \frac{0.5dx}{k_{insu,T_{i-1,n-1}}}} + \frac{T_{i-1,n-1} - T_{i,n}}{\frac{Inv_{O_f}}{h_{eff,T_{i-1},T_i}} + \frac{0.5dx}{k_{insu,T_{i,n}}}} + - \frac{T_{i,n} - T_{i+1,n+1}}{\frac{0.5dx}{k_{insu,T_i,n}} + \frac{0.5dx}{k_{insu,T_{i+1,n+1}}}} - h_{insu}\left(T_{i,n} - T_{i+1,n+1}\right) \right) \cdot \frac{dt}{\rho_{insu} c_{p,insu,T_{i,n}} \Delta x} \tag{B.13}$$

when both the previous and the next layer are thermal insulation on the unexposed side, for layers $31 \le n \le 53$ in the model, the calculated temperature is given by Equation B.14.

$$T_{iunexp,t+\Delta t,31\le n\le 53} = T_{i,n} + \left(\left(\frac{T_{i-1,n-1} - T_{i,n}}{\frac{0.5dx}{k_{insu,T_{i-1,n-1}}} + \frac{0.5dx}{k_{insu,T_{i,n}}}} - \frac{T_{i,n} - T_{i+1,n+1}}{\frac{0.5dx}{k_{insu,T_{i,n}}} + \frac{0.5dx}{k_{insu,T_{i-1,n-1}}}} + h_{insu}\left(T_{i,n} - T_{i+1,n+1}\right) \right) \cdot \frac{dt}{\rho_{insu} c_{p,insu,T_{i,n}} dx} \right) \tag{B.14}$$

The temperature in the last insulation layer on the unexposed side, i.e., when the next layer is the outer cladding, for layer n = 54 in the model, is expressed by Equation B.15.

$$T_{icladdunexp,i,t+\Delta t,n=54} = T_{i,n} + \left(\frac{T_{i-1,n-1} - T_{i,n}}{\frac{0.5dx}{k_{insu,T_{i-1,n-1}}} + \frac{0.5dx}{k_{insu,T_{i,n}}}} + h_{insu}\left(T_{i-1,n-1} - T_{i,n}\right) - \frac{T_{i,n} - T_{i+1,n+1}}{\frac{0.5dx}{k_{insu,T_{i,n}}} + \frac{1}{h_{eff,T_i,T_{i+1}}}} \right) \cdot \frac{dt}{\rho_{insu} c_{p,insu,T_{i,n}} dx} \tag{B.15}$$

The temperature in cladding on the unexposed side, for layer n = 55 in the model, is expressed by Equation B.16.

$$T_{claddunexp,i,t+\Delta t,n=55} = T_{i,n} + \left(\frac{T_{i-1,n-1} - T_{i,n}}{\frac{0.5dx}{k_{insu,T_{i-1,n-1}}} + \frac{1}{h_{eff,T_i,T_{i+1}}}} \right) \cdot \frac{dt}{\rho_s c_{p,s,T_{i,n}} l_{cladd}} \quad (B.16)$$

The effective heat transfer coefficient as a function of temperature is expressed by Equation B.17.

$$h_{eff,i} = \varepsilon\sigma \frac{(T_{i-1})^4 - (T_i)^4}{T_{i-1} - T_i} + h_s \quad (B.17)$$

The heat capacity of stainless steel as a function of temperature is expressed by Equation B.18 (Franssen and Real, 2015).

$$c_{p,s} = 1.340 \cdot 10^{-7} T^3 - 4.008 \cdot 10^{-4} T^2 + 4.690 \cdot 10^{-1} T + 349.075 \quad (B.18)$$

where T is the temperature in K.

The carbon steel heat capacity as a function of temperature is expressed by Equation B.19 (Franssen and Real, 2015).

For $T < 600$ °C:

$$c_{p,cs} = 2.220 \cdot 10^{-6} T^3 - 3.509 \cdot 10^{-3} T^2 + 2.193 T + 42.519 \quad (B.19)$$

where T is the temperature in K.

The heat capacity for the thermal insulation is expressed by Equations B.20 and B.21 and is based on the composition of the thermal insulation, as documented by Gunnarshaug et al. (2021).

For $T \leq 574$ °C:

$$c_{p,insu} = 2.7427 \cdot 10^{-6} T^3 - 5.530 \cdot 10^{-3} T^2 + 4.1913\, T - 52.826 \quad (B.20)$$

And for $T > 574$ °C:

$$c_{p,insu} = 0.1301 T + 1019.2166 \quad (B.21)$$

where T is the temperature in K.

Accounting for the sintered fraction of the thermal insulation and the corresponding radiation through the different insulation layers, the radiated heat through the insulation layers is expressed by Equation B.22.

$$\Delta Q_{rad,i,t+\Delta t} = \varepsilon\sigma \left((T_{cladd})^4 - (T_i)^4 \right) \cdot \left(A_{f,T_{i-1}} - A_{f,T_i} \right) \quad (B.22)$$

where T is the temperature (K) and A_f is the sintered fraction, expressed by Equations B.23 to B.26 (Gunnarshaug et al. (2021)).

For $T \leq 700$ °C:

$$A_f = 0 \quad (B.23)$$

for 700 °C $< T \leq$ 1140 °C

$$A_f = 1 - \left(-8.201 \cdot 10^{-5} T + 1.069 \right) \quad (B.24)$$

for 1140 °C $< T \leq$ 1200 °C:

$$A_f = 1 - \left(-1.023 \cdot 10^{-2}\, T + 15.406 \right) \quad (B.25)$$

For $T \leq 1200$ °C:

$$A_f = 0.7 \quad (B.26)$$

where T is the temperature in K.

References

API, 2014. API RP 583. In: Recommended Practice 583: Corrosion under Insulation and Fireproofing, first ed. American Petroleum Institute (API), Washington, DC, USA.

Bahadori, A., 2014. Thermal Insulation Handbook for the Oil, Gas, and Petrochemical Industries. Elsevier Science & Technology, Saint Louis.

Bakka, M.S., Eriksen, B., Johansen, O.J., Oltedal, H.L., Log, T., Rogde, S., 2021. Brann I Luftinntak På Gassturbin GTG4, Hammerfest LNG 20.09.2020 [Fire in Air Gas Turbine GTG4 Air Intake, Hammerfest LNG, 20.09.2020]. https://www.equinor.com/content/dam/statoil/documents/newsroom-additional-documents/news-attachments/endelig-rapport-coa-gransking-hlng-brann.pdf.

Bjørge, J.S., Gunnarshaug, A., Log, T., Metallinou, M.-M., 2018. Study of industrial grade thermal insulation as passive fire protection up to 1200 °C. Saf. Now. 4 (3), 41. https://doi.org/10.3390/safety4030041.

Bjørge, J.S., Metallinou, M.-M., Kraaijeveld, A., Log, T., 2017. Small Scale Hydrocarbon Fire Test Concept. https://doi.org/10.3390/technologies5040072.

Choi, J.-Y., Beyeon, S.-H., 2021. Overview of the legal design basis for passive fire protection in korea and the direction of further development. Sustainability 13, 1674. https://doi.org/10.3390/su13041674.

Drysdale, D., 2011. An Introduction to Fire Dynamics, Third Edition, third ed. Wiley, Chichester, West Sussex, U.K.

Equinor, 2019. The Insulation Handbook, p. TR1660.

Equinor, 2020. Performance Standards for Safety Systems and Barriers—Onshore; TR2237. Tysværvåg, Norway. Equinor.

Franssen, J.-M., Real, P.V., 2015. Fire Design of Steel Structures: Eurocode 1: Actions on Structures Part 1-2 – Actions on Structures Exposed to Fire, Eurocode 3: Design of Steel Structures Part 1-2 – General Rules – Structural Fire Design, second ed. European Convention for Constructional Steelwork, Portugal.

Gunnarshaug, A., Metallinou, M.M., Log, T., 2020. Study of industrial grade thermal insulation at elevated temperatures. Materials 13 (20), 4613. https://doi.org/10.3390/ma13204613.

Gunnarshaug, A., Metallinou, M.-M., Log, T., 2021. Industrial thermal insulation properties above sintering temperatures. Materials 14 (16), 4721. https://doi.org/10.3390/ma14164721.

Hallan, B., Rundell, L.-R., Thorsen, A.J., Steinbakk, A.-H., Sundby, T., 2021. *Report Of the Investigation of a Fire in the Air Intake of GTG4 at Hammerfest LNG*. Ptil. www.ptil.no/contentassets/3391c6686b2b4265abe8585294151335/2020_1862_rapport-equinor-hammerfest-lng-gransking-eng.pdf.

Handal, E.S., Sandvik, O.-I., de Jong, H., Bondevik, T.B., Ovesen, R.V., 2021. Brann i kompressorhus på tjeldbergodden (fire in compressor house at tjeldbergodden), equinor corporate investigation report. https://www.equinor.com/content/dam/statoil/documents/newsroom-additional-documents/news-attachments/endelig-rapport-coa-gransking-tbo-brann.pdf.

ISO (International Organization for Standardization), 2015. Plastics—Determination of Thermal Conductivity and Thermal Diffusivity—Part 2: Transient Plane Heat Source (Hot Disc) Method; ISO 22007:2. International Organization for Standardization, Geneva, Switzerland.

Kissinger, H.E., 1956. Variation of peak temperature with heating rate in differential thermal analysis. J. Res. Natl. Bur. Stand. 57, 217–221.

Lai, F., Leng, M., Li, J., Liu, Q., 2020. The crystallization behaviors of SiO2-Al2O3-CaO-MgO-TiO2 glass-ceramic systems. Crystals 10 (9), 794. https://doi.org/10.3390/cryst10090794.

Landro, E., Haug, B.A., Hjellestad, K.I., Mihajlovic, D., Sande, E., Steinbakk, A.H., 2021. Report Following the Investigation of a Turbine Breakdown with Subsequent Fire at Tjeldbergodden on 2 December 2020. https://www.ptil.no/contentassets/d7cb364377b741a597c8b85dd06c8ce9/2020_2201-rapport-eng-gransking-equinor-tjeldbergodden.pdf.

Log, T., Gunnarshaug, A., 2022. Analysis of a costly fiberglass-polyester air filter fire. Energies 15 (20), 7719. https://doi.org/10.3390/en15207719.

Matusita, K., Sakka, S., 1980. Kinetic study of crystallization of glass by differential thermal analysis-criterion on application of kissinger plot. J. Non-Cryst. Solids 38, 741–746.

Olsen, H., Sjöström, J., Jansson, R., Anderson, J., 2013. Thermal properties of heated insulation materials, 24–26 June 2013. In: Proceedings of the 13th International Fire and Engineer Conference. INTERFLAM, London, UK.

Ozawa, T., 1971. Kinetics of non-insuthermal crystallization. Polymer 12 (3), 150–158.

Rockwool, 2023. Retrieved 2023.03.23 from. https://www.rockwool.com/west-virginia/factory-operations-and-production.

Scandpower, 2004. Guidelines for the Protection of Pressurised Systems Exposed to Fire.

Shao, H., Liang, K., Peng, F., 2004. Crystallization kinetics of MgO–Al2O3–SiO2 glass-ceramics. Ceram. Int. 30 (6), 927–930. https://doi.org/10.1016/j.ceramint.2003.10.015.

Sjöström, J., Jansson, R., 2012. Measuring thermal material properties for structural fire engineering, 22–27 July 2012. In: Proceedings of the 15th International Conference on Experimental Mechanics, ICEM15, Porto, Portugal.

Standard Norway, 2018. S-001 Technical Safety. Oslo, Norway: NORSOK Standard, fifth ed. Norwegian Technology Standards Institution.

Unifrax, 2017. FyreWrap LT Blanket. Retrieved 2022.12.06 from. https://www.unifrax.com/en-uk/product/fyrewrap-lt-blanket/.